Advanced Functional Materials

ADVANCED FUNCTIONAL MATERIALS
www.afm-journal.de

RESEARCH ARTICLE

Ultra-Low-Energy $NbOI_2$ Synaptic Transistors for Neuromorphic Computing and Closed-Loop Human-Machine Interaction

Kun Lv[1] | Ping Chen[1] | Yanjie Kong[1] | Yeming Chen[1] | Ni Zhang[1] | Haowen Tang[1] | Xiaofeng Liu[2] | Yanqi Gu[3] | Xiao Zhang[4] | Caofeng Pan[3]

[1]Center on Nanoenergy Research, Guangxi Key Laboratory for Relativistic Astrophysics, School of Physical Science and Technology, Guangxi University, Nanning, China | [2]School of Materials Science and Engineering, Zhejiang University, Hangzhou, China | [3]Institute of Atomic Manufacturing, Beihang University, Beijing, China | [4]State Key Laboratory of Information Photonics and Optical Communications, School of Physical Science and Technology, Beijing University of Posts and Telecommunications, Beijing, China

Correspondence: Ping Chen (chenping@gxu.edu.cn) | Xiao Zhang (zhangxiaobupt@bupt.edu.cn) | Caofeng Pan (pancaofeng@buaa.edu.cn)

Received: 26 November 2025 | **Revised:** 7 February 2026 | **Accepted:** 9 February 2026

Keywords: closed-loop human-machine interaction | $NbOI_2$ | opto-electronic synapses | robotic arm control | ultralow energy consumption

ABSTRACT

As the bottleneck of energy efficiency associated with the separation of storage and computation in the von Neumann architecture becomes increasingly restrictive, brain-inspired electronic devices based on 2D materials are emerging as promising candidates for next-generation information processing. Here, a top-gate tri-terminal optoelectronic synapse based on 2D $NbOI_2$ is demonstrated. Stable inhibitory postsynaptic current (IPSC) modulation and paired-pulse depression (PPD) behaviors are successfully emulated for the first time in $NbOI_2$ devices. The device achieves an ultralow single-spike energy consumption, comparable to that of natural biological synapses (~10 fJ). Under hybrid optical-electrical stimulation, it exhibits long-term potentiation and depression (LTP/LTD), showing versatile synaptic plasticity. An artificial neural network constructed using its synaptic properties achieves classification accuracies of 93.61% and 84.57% on the MNIST and Fashion-MNIST datasets, respectively. Furthermore, a closed-loop human-machine interaction system inspired by the vision-neural-motor pathway is established by exploiting the accumulative photocurrent memory of $NbOI_2$ synapses. Multi-channel robotic arm control is also realized, highlighting the scalability of $NbOI_2$ optoelectronic synapses for complex collaborative tasks. This work demonstrates the dual potential of $NbOI_2$ optoelectronic synapses in neuromorphic computing and intelligent human-machine interaction, offering insights for the development of energy-efficient brain-inspired electronics.

1 | Introduction

With the rapid development of artificial intelligence, big data, and human-machine interaction technologies, information processing systems have encountered unprecedented challenges in terms of performance, energy efficiency and intelligence [1–4]. The conventional von Neumann architecture based on the physical separation of perception, storage, and computation units has suffered from the "memory wall" effect, which results in increasingly insufficiency of real-time responsiveness, multimodal integration, and ultralow power operation [5, 6]. In stark contrast, the human brain exhibits remarkable features,

Kun Lv and Ping Chen have contributed equally to this work.

including extremely low energy consumption, high fault tolerance and outstanding adaptive learning capabilities, integrating multi-modal sensory inputs through massively parallel processing with approximately 10^{12} neurons interconnected by about 10^{15} synapses [7]. Biological synapses, serving as the fundamental connection units between neurons, enable the integration of information storage and processing via neurotransmitter release and dynamic synaptic weight modulation, thereby providing the essential basis for learning, memory and reasoning [8, 9]. Therefore, artificial synaptic devices have attracted growing attention with capable of executing storage and computation simultaneously [10, 11]. In particular, 2D materials are regarded as ideal candidates for constructing high-performance opto-electronic synapses with atomic-scale thickness, excellent gate controllability and unique opto-electronic properties [12–21].

Among various 2D semiconductors, $NbOI_2$ stands out as an emerging 2D ferroelectric semiconductor and exhibits peculiar performance in opto-electronic detection, piezoelectric sensing and nonlinear optics benefited from its moderate bandgap, strong piezoelectric/ferroelectric responses, pronounced in-plane anisotropy and robust second-harmonic generation (SHG) [22–29]. In this year, Zhai et al. first realized artificial synapse based on $NbOI_2$ by exploiting the multiphysics coupling characteristics. They proposed a 2D piezoelectric-ferroelectric-opto-electronic (PFOE) artificial synapse, which enabled integrated regulation of visual and tactile signals within a $NbOI_2$ device. Based on the synergistic action of light and strain, fingerprint image clarity and recognition accuracy were improved through visual-tactile information fusion [30]. Subsequently, the same group developed a 2D time-stretching anisotropic synapse (2D TSAS), by leveraging the intrinsic in-plane anisotropy of $NbOI_2$ and its multi-channel excitation-relaxation dynamics. Those encoding and temporal integration of polarization features facilitated handling brightness contrasts in high dynamic range (HDR) visual environments. The 2D TSAS achieved recognition accuracies of approximately 95% on both the NWPU-RESISC45 and MNIST datasets [31]. Although these advances clearly demonstrate the potential of $NbOI_2$ in artificial synapses and multimodal perception, the reported devices still relied on optical or strain stimuli for modulation. Systematic investigations of $NbOI_2$ based artificial synapses responsive to electrical impulses remain unexplored, which is the fundamental information carriers in biological neural systems. Moreover, current research mostly confined to proof-of-concept demonstrations at the device level. How to extend synaptic plasticity toward bionic systems and achieve a continuous process from environmental perception to action execution still demands an in-depth exploration.

Herein, a top-gate tri-terminal opto-electronic synapse device based on $NbOI_2$ was demonstrated. Stable inhibitory synaptic currents (IPSCs) and paired-pulse depression (PPD) were realized with the stimulation of electrical pulses for the first time in $NbOI_2$-based devices. Notably, the device exhibits an ultralow single-spike energy consumption of ~89 aJ, which is two orders of magnitude lower than that of natural biological synapses (~10 fJ), highlighting its superior energy efficiency. In addition, bidirectional plasticity regulation in the form of long-term potentiation and depression (LTP/LTD) were demonstrated under dual-mode opto-electrical pulse stimulation. Recognition accuracies of 93.61% and 84.57% for image classification tasks, enabled by embedding weight update functions extracted from the LTP/LTD curves into artificial neural networks (ANN), were achieved on the MNIST and Fashion-MNIST datasets, respectively, thereby validating the potential for neuromorphic computing. Furthermore, a closed-loop human-machine interaction system inspired by the vision-neural-motor pathway was constructed, which was used to drive a robotic arm to autonomously approach and grasp target objects where front-end binocular cameras combined with a YOLO-v8 neural network performed real-time target detection and localization, and $NbOI_2$ opto-electronic synapses served as the processing and memory core. Besides, multi-channel robotic hand control based on $NbOI_2$ opto-electronic synapses was realized, validating not only the feasibility of independent finger actuation but also the scalability of these devices in complex human-machine collaboration scenarios. Collectively, this work establishes a comprehensive neuromorphic application pathway for $NbOI_2$ spanning materials, devices, algorithms, and system-level integration, providing novel strategies for next-generation brain-inspired hardware aimed at visual perception and intelligent human-machine collaboration.

2 | Results and Discussion

2.1 | Design Concept of the $NbOI_2$ Opto-Electronic Synapses

In biological hand grip control with visual guidance systems, light signals, scattered from external objects enter into the eye with refraction and pupil adjustment, are focused onto the retina, and subsequently converted into electrical signals by photoreceptor cells. These electrical signals are transmitted via neurons and synapses to the visual cortex of the brain, where recognition and decision-making occur. The feedback signals then propagate along motor pathways to effector muscles, enabling the limbs to progressively approach and eventually grasp the target object (Figure 1a) [32]. Inspired by this vision-motor pathway, $NbOI_2$ was employed to realize analogous information processing and execution functions.

As a transition-metal dihalide oxide, $NbOI_2$ possesses a moderate bandgap (1.6–1.9 eV) [30], with its fundamental structural unit being a distorted $[NbO_2I_4]$ octahedron. In the crystal lattice, $NbOI_2$ layers are stacked along the *a*-axis through van der Waals interactions, while O-Nb-O and I-Nb-I chains extend along the *b*- and *c*-axis, respectively [22]. The displacement of Nb atoms from the octahedral center induces spontaneous polarization along the Nb—O bond direction (Figure 1b), resulting in a built-in electric field [27]. The electric field suppresses photogenerated carrier recombination and increases carrier lifetime, thereby providing the physical basis for brain-like synaptic plasticity in artificial opto-electronic synapses [30]. Moreover, the weaker Nb—I bond strength along the *c*-axis, compared with the stronger Nb—O bonding along the *b*-axis, results in a preferred cleavage orientation along the *b*-axis during mechanical exfoliation [22]. Consequently, exfoliated $NbOI_2$ flakes typically exhibit rectangular or elongated morphologies with nearly vertical edges, facilitating rapid identification of crystallographic orientation under optical microscopy. EDS analysis of exfoliated $NbOI_2$ flakes reveals uniform spatial distribution and compositional consistency of Nb and I elements across the samples (Figure S1a).

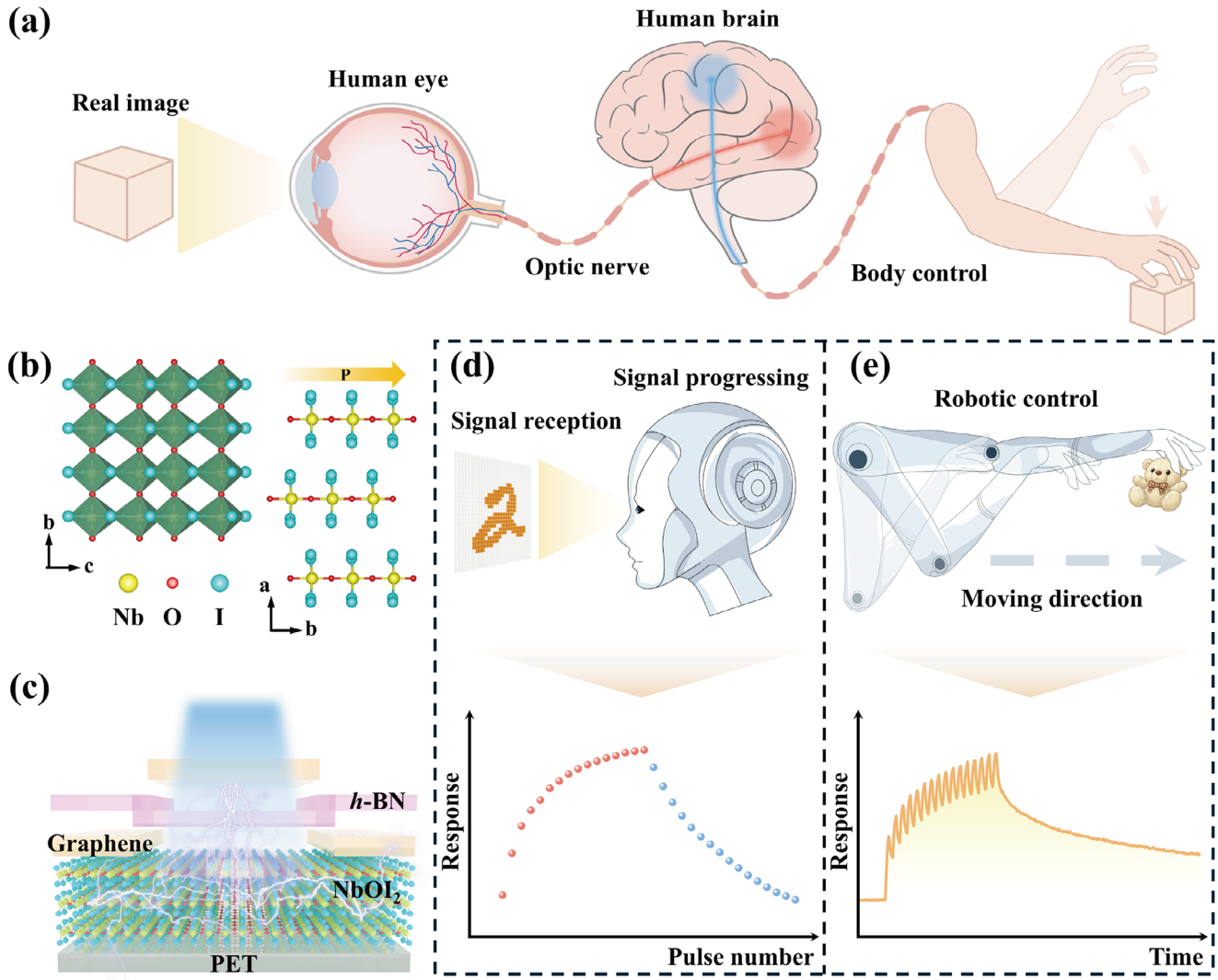

FIGURE 1 | Design concept of device implementation for the $NbOI_2$-based optoelectronic synapses. (a) Schematic illustration of signal transmission in human neural pathways. (b) Crystal structure of $NbOI_2$. (c) Device architecture of a three-terminal top-gate $NbOI_2$-based optoelectronic synapse, employing graphene electrodes and *h*-BN encapsulation. (d) Nonlinear weight-update parameters extracted from LTP/LTD curves, which are mapped into weight update rules and embedded into a fully connected ANN to simulate visual perception and classification. (e) The accumulated photocurrent memory effect under optical pulse stimulation enables closed-loop control of the robotic arm, achieving progressive extension and grasping actions.

To further evaluate the crystal quality, Raman spectroscopy was performed on the $NbOI_2$ flakes. Five characteristic peaks (P_1-P_5) were observed centered at 101, 205, 270, 520, and 608 cm^{-1} (Figure S1b) [27]. The peaks at 101 and 608 cm^{-1} correspond to the symmetric bending vibration and asymmetric stretching vibration of the Nb—I bond, respectively. Those peaks at 205 and 270 cm^{-1} are attributed to the collective vibrational modes of the [NbO_2I_4] octahedron, while the peak at 520 cm^{-1} originates from the symmetric bending vibration of the Nb—O bond, confirming the structural integrity of the $NbOI_2$ crystal [27, 33]. In addition, high-resolution transmission electron microscopy (HRTEM) (Figure S1c) revealed clear lattice fringes with an interplanar spacing of approximately 0.27 nm, corresponding to the $d(\bar{1}12)$ spacing of monoclinic $NbOI_2$, indicating a well-ordered crystal structure [27, 35]. X-ray diffraction (XRD) patterns (Figure S1d) agreed well with the standard PDF data, confirming the monoclinic phase and phase purity of the $NbOI_2$ samples [26, 27].

To fully exploit the intrinsic in-plane polarization of $NbOI_2$, a three-terminal top-gate opto-electronic synapse device was constructed on a flexible PET substrate, aligned along the *b*-axis of $NbOI_2$. The device employed $NbOI_2$ thin flakes as the channel, while graphene served as the source, drain, and top-gate electrodes. *h*-BN was used as an inert encapsulation layer to stabilize the interface and suppress environmental oxidation [34, 35], presenting a van der Waals hetero-integrated top-gate architecture with an $NbOI_2$ thickness of approximately 35 nm (Figure 1c; Figure S2b). HRTEM further revealed well-defined and atomically clean interfaces between the $NbOI_2$, graphene, and *h*-BN layers, indicating high-quality van der Waals integration (Figure S2c). The device exhibits pronounced photocurrent responses under red, green, and blue light illumination, confirming its multi-band sensitivity analogous to biological visual synapses (Figure S3). In addition, a clear clockwise hysteresis window is observed in the I_{DS}-V_{GS} characteristics, indicating excellent charge storage and retention capability, thereby highlighting the

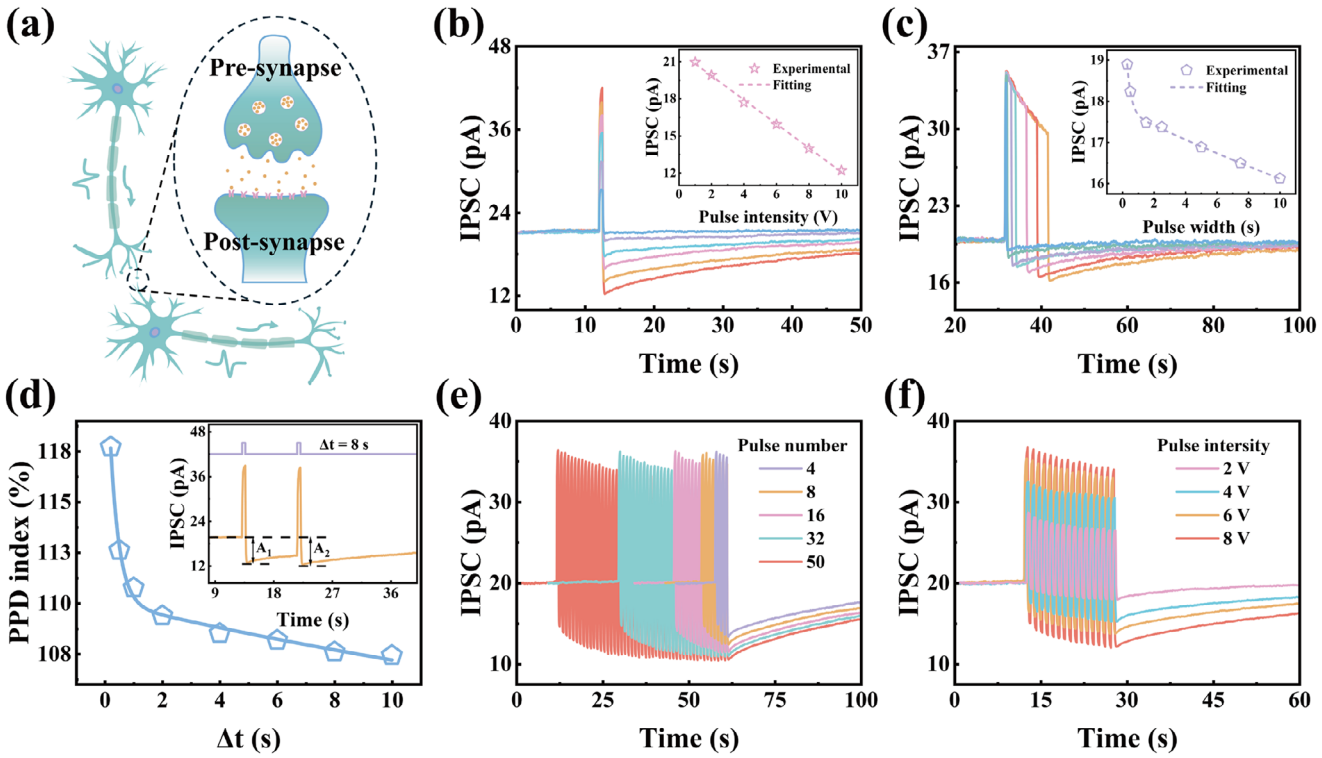

FIGURE 2 | Electrical-pulse-modulated inhibitory synaptic plasticity. (a) Schematic illustration of biological synaptic information transmission. (b) IPSC responses of the device under different amplitudes of positive gate voltage pulses (2, 4, 6, 8, and 10 V, pulse width = 0.5 s, V_{DS} = 0.1 V). Inset: dependence of IPSC peak on pulse amplitude. (c) IPSC responses under different pulse widths of positive gate voltage pulses (0.3, 0.5, 1.5, 2.5, 5, 7.5, and 10 s, pulse amplitude = 5 V, V_{DS} = 0.1 V). Inset: dependence of IPSC peak on pulse width. (d) Variation of the PPD indices with pulse interval (0.2–10 s, pulse amplitude = 8 V, pulse width = 0.5 s, V_{DS} = 0.1 V). Inset: representative PPD response triggered by two consecutive electrical pulses (pulse amplitude = 8 V, pulse width = 0.5 s, pulse interval = 8 s, V_{DS} = 0.1 V). (e) Transition from STD to LTD as the number of electrical pulses increases (pulse amplitude = 8 V, pulse width = 0.5 s, pulse interval = 0.5 s, V_{DS} = 0.1 V). (f) Transition from STD to LTD with increasing pulse amplitude (number of pulses = 16, pulse width = 0.5 s, pulse interval = 0.5 s, V_{DS} = 0.1 V).

device's potential for non-volatile memory applications and artificial synapses (Figure S4). The nonlinear parameters extracted from the LTP and LTD plasticity of artificial synapses could be incorporated into weight update rules of ANN to enable reliable simulation of visual perception and image classification (Figure 1d) [36]. Furthermore, a cumulative photocurrent memory effect can mimic the neural process of motor neuron excitation and muscle contraction under continuous visual stimuli, allowing for controlled progressive extension and grasping motions of a robotic arm (Figure 1e).

2.2 | Electrical-Pulse-Modulated Inhibitory Synaptic Plasticity

The biological synapse, which serves as the fundamental unit for information transmission between neurons, consists of the presynaptic membrane, synaptic cleft, and postsynaptic membrane. When an action potential arrives at the presynaptic terminal, neurotransmitters are released from the presynaptic membrane, diffuse across the synaptic cleft, and subsequently bind to receptors on the postsynaptic membrane. This process induces either excitatory postsynaptic currents (EPSCs) or IPSCs, thereby completing neural signal transmission (Figure 2a) [37]. The plasticity of these postsynaptic currents modulated by electrical pulses plays a pivotal role in modulating synaptic strength and underlies essential brain functions such as learning and memory [38].

To systematically evaluate the synaptic behavior of the $NbOI_2$-based three-terminal opto-electronic synapse device with electrical simulation, its current response and associated plasticity characteristics under positive gate-voltage pulse stimulation were investigated (all measurements were conducted in dark-field mode at V_{DS} = 0.1 V). When a single electrical pulse was applied through the top gate, the device exhibited a clear IPSCs (Figure 2b), which was first observed in $NbOI_2$ synapses. The instantaneous current after pulse termination fell below the initial baseline and subsequently recovered gradually. With increasing pulse amplitude, the IPSC peak, defined as the instantaneous minimum current following pulse withdrawal, decreased from 21 to 12 pA, indicating progressively enhanced suppression. This dependence of IPSC amplitude on gate-voltage strength demonstrates the device's voltage-dependent inhibitory plasticity (inset in Figure 2b). The underlying mechanism can be attributed to the combined effects of the gate-induced electric field on carrier distribution and defect trapping within the $NbOI_2$ flake, such as iodine-vacancies [35, 39, 40]. When a positive gate-voltage is applied, electrons are driven into the channel, producing an initial current increase, accompanying with trapping partial electrons in iodine defects. Upon removal of the gate pulse, the free-carrier density in the channel recovers quickly, whereas

trapped electrons cannot de-trap instantaneously. This transient imbalance causes the current to drop below its initial value, manifesting as an IPSC. Subsequently, the gradual release of trapped electrons enables recovery of the current to the baseline level (Figure S5). And the increased pulse amplitude induces a higher electron concentration and a larger number of trapped electrons in iodine defects, leading to a progressively enhanced suppression of IPSC. Beyond pulse amplitude, the duration of the electrical pulse also significantly influences the synaptic behavior. As shown in Figure 2c, a single positive gate pulse with varying widths of 0.3, 0.5, 1.5, 2.5, 5, 7.5, and 10 s was applied with a fixed amplitude of 5 V. With increasing pulse width, the IPSC peak gradually decreased from 19 to 16 pA, indicating a stronger suppression effect. The inset further illustrates the dependence of IPSC amplitude on pulse width, confirming the temporal tunability of inhibitory plasticity.

Paired-pulse plasticity behavior was examined to validate the synaptic characteristics of the device under temporally correlated stimuli. In biological synapses, paired-pulse plasticity is a typical manifestation of short-term plasticity (STP), reflecting the ability to process consecutive stimuli. It describes two postsynaptic spikes generated by two successive inputs. If the current amplitude triggered by the second pulse exceeds that of the first, the behavior is defined as paired-pulse facilitation (PPF). Conversely, it is referred to as PPD. The quantitative index for paired-pulse plasticity is given by [41–44]:

$$PPD\,(PPF)\,index = \frac{A_1}{A_2} \times 100\% \tag{1}$$

where A_1 and A_2 represent the IPSCs triggered by the first and second pulses, respectively. The dependence of the PPD indices on the pulse interval Δt can be fitted by a double-exponential function [45, 46]:

$$PPD\,(PPF) = 1 + C_1 \exp\left(-\frac{\Delta t}{\tau_1}\right) + C_2 \exp\left(-\frac{\Delta t}{\tau_2}\right) \tag{2}$$

where C_1 and C_2 correspond to the initial magnitudes of rapid and slow decay, and τ_1 and τ_2 are the respective relaxation time constants. As shown by the inset in Figure 2d, the device exhibited PPD behavior under two consecutive positive gate-voltage pulses (amplitude: 8 V; width: 0.5 s). As the interval Δt increased from 0.2 to 10 s, the PPD indices monotonically decreased from 117% to 107%. Fitting of the results yielded time constants of $\tau_1 = 0.3$ s and $\tau_2 = 29.98$ s.

After confirming the presence of short-term plasticity, the long-term plasticity characteristics of the device under multi-pulse stimulation were investigated. With a constant gate voltage amplitude of 8 V, electrical pulse sequences of 4, 8, 16, 32, and 50 pulses were applied. For a small number of pulses, limited electron trapping in the $NbOI_2$ flake resulted in short-term depression (STD) (Figure 2e). With increasing pulse number, more electrons were captured, leading to a pronounced current reduction and the emergence of LTD, thereby demonstrating the transition from STD to LTD through modulation of pulse count [47]. Furthermore, the influence of stimulation intensity on LTD regulation was examined. At a fixed pulse number of 16, electrical pulses with amplitudes of 2, 4, 6, and 8 V were applied. Increasing gate-voltage amplitude similarly enabled the transition from STD to LTD (Figure 2f), highlighting the dual tunability of inhibitory synaptic plasticity by both pulse number and pulse intensity.

The results of the electrical stimulation experiments reveal the unique capability of the $NbOI_2$-based devices in regulating inhibitory synaptic plasticity. Nevertheless, efficient information processing in biological neural networks relies not only on inhibitory modulation but also on the dynamic cooperation with excitatory signaling. Therefore, systematic investigation of the device's excitatory synaptic behavior under optical pulse stimulation is essential in order to assess comprehensively its brain-like functional potential.

2.3 | Light-Pulse-Modulated Excitatory Synaptic Plasticity

Single-spike energy consumption was first characterized to evaluate the excitatory synaptic plasticity and energy efficiency of the device under optical stimulation, followed by a systematic investigation of EPSC dependence on optical parameters and plasticity behavior. A photocurrent of 1.14 pA in the device was induced by a single 405 nm light pulse (optical power density: 2.8 mW cm^{-2}; pulse width: 0.1 s) with source-drain voltage at 1 mV (Figure 3a). The electrical energy consumption per synaptic event was calculated according to the following equation [48, 49]:

$$E = \int V_{DS} \cdot I_{DS} dt \tag{3}$$

where V_{DS} is the source–drain voltage, I_{DS} is the postsynaptic current, and t is the pulse duration. The energy consumption per synaptic event was calculated to be 89 aJ, which is approximately two orders of magnitude lower than that of natural biological synapses (~10 fJ) and lower than the energy consumption from those typical 2D materials (Table S1), thereby demonstrating the ultralow-power characteristics of the $NbOI_2$ opto-synapse [50]. It should be noted that such an ultralow-energy is an inherent trade-off between energy efficiency and signal stability in optoelectronic synaptic devices (Figure S6).

After confirming the ultralow energy consumption of single optical pulses, the dependence of EPSCs on external light-stimulation was systematically investigated. When single light pulses with different intensities (2.8, 6.5, 9.1, 14.3, and 19.2 mW cm^{-2}; pulse width = 0.3 s) were applied to the device (Figure 3b), the EPSC rapidly increased during illumination and gradually decayed toward its initial state after removing the light, where the energy consumption per synaptic event reached 6.65 fJ with the optical power density at 2.8 mW cm^{-2}. With increasing light intensity, the EPSC peak rose progressively, as further illustrated by the intensity dependence in the inset of Figure 3b. This behavior can be attributed to the synergistic interaction between photo-generated carriers and defect trapping [35, 39, 40]. Upon illumination, abundant photo-generated electrons and holes are produced in the channel, resulting in a sharp increase in current. Simultaneously, intrinsic defect states within $NbOI_2$ capture part of these carriers. Once ceasing illumination, electrons and holes rapidly recombine, resulting in a sharp decrease in current. However, electrons trapped at defect states are released slowly, which reduce current decay and prevented an immediate return

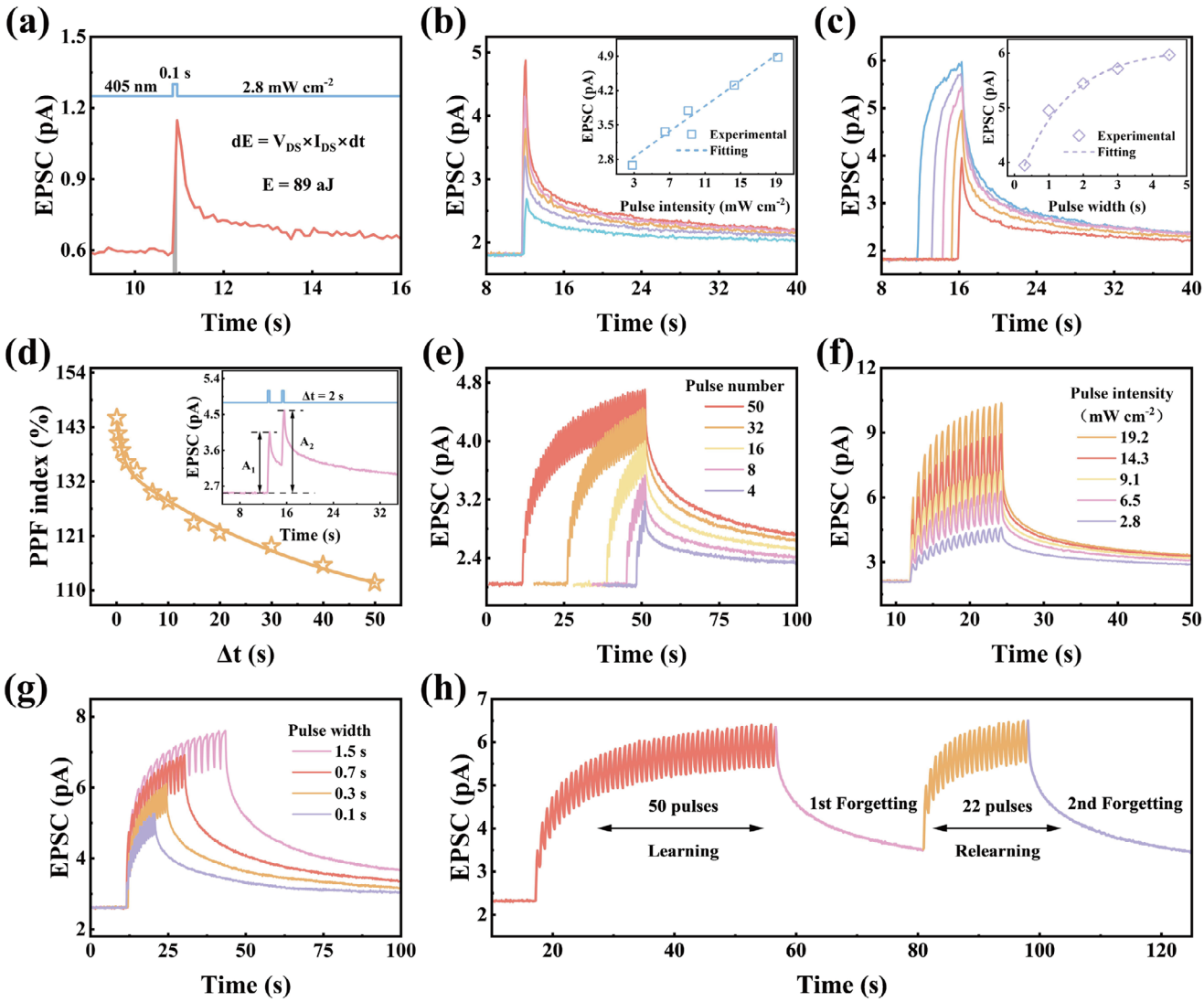

FIGURE 3 | Light-pulse-modulated excitatory synaptic plasticity of the $NbOI_2$-based optoelectronic synapses. (a) EPSC response under a single light pulse (V_{DS} = 0.001 V, λ = 405 nm, optical power density = 2.8 mW cm^{-2}, pulse width = 0.1 s). (b) EPSC responses under increasing optical power densities (2.8, 6.5, 9.1, 14.3, and 19.2 mW cm^{-2}; V_{DS} = 0.01 V, λ = 405 nm, pulse width = 0.3 s). Inset: dependence of EPSC peak on optical power density. (c) EPSC responses under different light pulse widths (0.3, 1, 2, 3, and 4.5 s; V_{DS} = 0.01 V, λ = 405 nm, optical power density = 9.1 mW cm^{-2}). Inset: dependence of the EPSC peak on pulse width. (d) Variation of the PPF indices with light pulse interval Δt (0.1–50 s; optical power density = 9.1 mW cm^{-2}, pulse width = 0.3 s). Inset: representative PPF response triggered by two consecutive light pulses (V_{DS} = 0.01 V, λ = 405 nm, optical power density = 9.1 mW cm^{-2}, pulse width = 0.3 s, pulse interval = 2 s). (e) Transition from STP to LTP with increasing numbers of light pulses (V_{DS} = 0.01 V, λ = 405 nm, optical power density = 2.8 mW cm^{-2}, pulse width = 0.3 s, pulse interval = 0.3 s). (f) Transition from STP to LTP with increasing optical power density (V_{DS} = 0.01 V, λ = 405 nm, number of pulses = 16, pulse width = 0.3 s, pulse interval = 0.3 s). (g) Transition from STP to LTP with increasing light pulse width (V_{DS} = 0.01 V, λ = 405 nm, optical power density = 6.5 mW cm^{-2}, number of pulses = 16, pulse interval = 0.3 s). (h) Simulation of the learning-forgetting-relearning behavior.

to the original state (Figure S7). Furthermore, EPSC gradually intensified with increasing pulse duration (Figure 3c) by varying the pulse width (0.3, 1, 2, 3, and 4.5 s) at fixed optical power density at 9.1 mW cm^{-2}, revealing that the device featured typical pulse-duration-dependent plasticity. Importantly, the device exhibited both intensity-dependent and pulse-duration-dependent excitatory behavior. These dependencies of the $NbOI_2$ optical synapses were consistently under the excitation by 520 and 650 nm (Figures S8 and S9). Comparative analysis across different wavelengths further confirmed that the device maintains stable and reproducible opto-synaptic performance across the visible spectral region (Figure S10).

Then, short-term plasticity was further examined by simulating PPF with applying two consecutive optical pulses. The peak current A_2 induced by the second pulse was significantly larger than the peak current A_1 generated by the first pulse. As the pulse interval gradually increased from 0.1 to 50 s, the PPF indices decreased from 145% to 111% (Figure 3d), and the decay behavior was well-fitted by a double-exponential decay function. The relaxation time constants were determined to be 0.58 s (τ_1) and 25.35 s (τ_2), matching well with the typical relaxation dynamics observed in biological synapses [51]. The observed PPF effect can be attributed to the accumulation of photo-generated carriers within the channel at shorter pulse

intervals, which enhances the device response to subsequent stimuli.

Human memory is generally categorized into short-term memory (STM) and long-term memory (LTM). At the neural synapse level, this process manifests as the transition from STP to LTP, which typically relies on repeated or intensified stimulation to achieve synaptic consolidation [52]. To emulate this process, 405 nm light pulses with fixed width (0.3 s), interval (0.3 s) and optical power density (2.8 mW cm^{-2}) were applied to the device. When the number of pulses was small (e.g. 4), only STP was observed, with EPSCs rapidly decaying to the original state within a short time. However, as the number of pulses increased to be 8, 16, 32, and 50, the EPSC amplitude enhanced progressively within the same decay period (Figure 3e), indicating a clear transition from STP to LTP. This result demonstrates that the conversion from STP to LTP conversion can be effectively modulated by increasing the number of optical pulses. Similarly, an increase in the optical power density (2.8–19.2 mW cm^{-2}) also enabled the transition from STP to LTP (Figure 3f) by fixing the pulse number (16), pulse width (0.3 s), and interval (0.3 s). In addition, increasing the optical pulse width (0.1, 0.3, 0.7, and 1.5 s) yielded the same transition from STP to LTP (Figure 3g) under constant optical power density (6.5 mW cm^{-2}), pulse count ($n = 16$), and pulse interval (0.3 s). These observations were verified consistently under 520 and 650 nm illumination, further confirming wavelength-independent excitatory plasticity and memory retention (Figures S11–S13). To further simulate higher-level cognitive processes, the device response was examined during forgetting and relearning cycles [53]. The $NbOI_2$ synapses exhibited a strong learning effect with a 50 pulses sequence under stimulation with optical pulses of width at 0.3 s, optical interval at 0.3 s and power density at 6.5 mW cm^{-2}. This was followed by a time-dependent decay of EPSCs, indicating the forgetting process. Followed by re-applying 22 pulses, the $NbOI_2$ synapses response not only recovered to the original level but also exceeded the first learning current, showing enhanced synaptic strength (Figure 3h). This behavior is in line with the Ebbinghaus forgetting curve that human memory can be rapidly restored and reinforced through review after partial forgetting. Such results further highlight the capability of the $NbOI_2$ opto-synapse to emulate "learning-forgetting-relearning" dynamics, thereby demonstrating its potential for mimicking advanced brain-like learning behaviors.

2.4 | Image Recognition Performance Based on ANN

To demonstrate neuromorphic computing inspired by biological vision, a three-layer fully connected ANN was constructed and employed to classify images from the 28 × 28 pixel MNIST and Fashion-MNIST datasets [54–56]. The ANN consists of an input layer, a hidden layer, and an output layer, where the input layer contains 784 neurons corresponding to the image pixels, the hidden layer consists of 512 neurons, and the output layer includes 10 neurons. All neurons are interconnected through synaptic weights (Figure 4a). In this framework, X_0-X_{783} represent the input pixel values of the image, while Y_0-Y_9 denote the output classes. For the MNIST dataset, Y_0-Y_9 correspond to digits from "0" to "9." For the Fashion-MNIST dataset, they correspond to the ten clothing categories such as T-shirts, trousers, shoes, and etc. Each dataset contains 60 000 training images and 10 000 testing images, which are used to evaluate recognition performance.

Considering that LTP and LTD are crucial to analog neuromorphic computation, where their linearity and dynamic conductance range are connected to ANN recognition accuracy directly. These weight update parameters were extracted by leveraging the device's plasticity behavior under dual-mode photo-electrical pulse stimulation. The device conductance increased progressively with adding the number of pulses, corresponding to LTP. Conversely, when electrical pulses were applied, the conductance gradually decreased with increasing pulse number, corresponding to LTD (Figure 4b). The nonlinearity (NL) of the weight update process was quantified by fitting the LTP and LTD curves by the following equations [57, 58]:

$$G_{n+1} = G_n + \alpha_p \exp\left(-\beta_p \frac{G_n - G_{min}}{G_{max} - G_{min}}\right) \quad (4)$$

$$G_{n+1} = G_n - \alpha_d \exp\left(-\beta_d \frac{G_n - G_{min}}{G_{max} - G_{min}}\right) \quad (5)$$

where G_n and G_{n+1} denote the conductance values for the nth and $(n+1)$th pulses, respectively. G_{min} and G_{max} are the minimum and maximum conductance values. α_p and α_d represent the step sizes on the potentiation and depression curves, respectively. β_p and β_d denote the NL coefficients of the potentiation and depression processes, respectively. The calculated β_p and β_d values were 3.06 and 2.15, respectively. During ANN training, synaptic weights follow the LTP update rule when the gradient is positive, whereas they follow the LTD update rule when the gradient is negative. Moreover, the cycling stability and symmetry of photo–electrical conductance modulation were evaluated (Figure S14), demonstrating excellent endurance.

Based on the extracted weight update parameters, synapse-derived weight update rules were embedded into an ANN to simulate image recognition tasks. Confusion matrices were presented with MNIST and Fashion-MNIST after 100 training epochs using these synapse-derived updates (Figure 4c,d). The strong consistency between predicted classes and ground-truth labels confirmed the network's effective classification capability for both datasets. A further comparison of classification performance between ideal weight updates—implemented using the Adam optimizer with cross-entropy loss backpropagation—and $NbOI_2$ synapses-derived weight updates is shown in Figure 4e. In both cases, classification accuracy improved progressively with increasing training epochs. After 100 epochs, the accuracies based on the $NbOI_2$ synapses reached 93.61% on MNIST and 84.57% on Fashion-MNIST. These results are only slightly lower than the corresponding ideal accuracies of 98.37% and 89.61%, respectively, thereby fully demonstrating the feasibility of $NbOI_2$-based opto-electronic synapses for ANN classification tasks.

To assess the noise tolerance of the ANN, additive random noise with varying intensities was introduced into both the training and test datasets with the noise level gradually increased from 0% to 40% (Figure 4f). It was observed that the classification accuracy on the MNIST dataset decreased from 93.61% to 89.08% as the noise intensity increased from 0% to 40%, corresponding to a drop

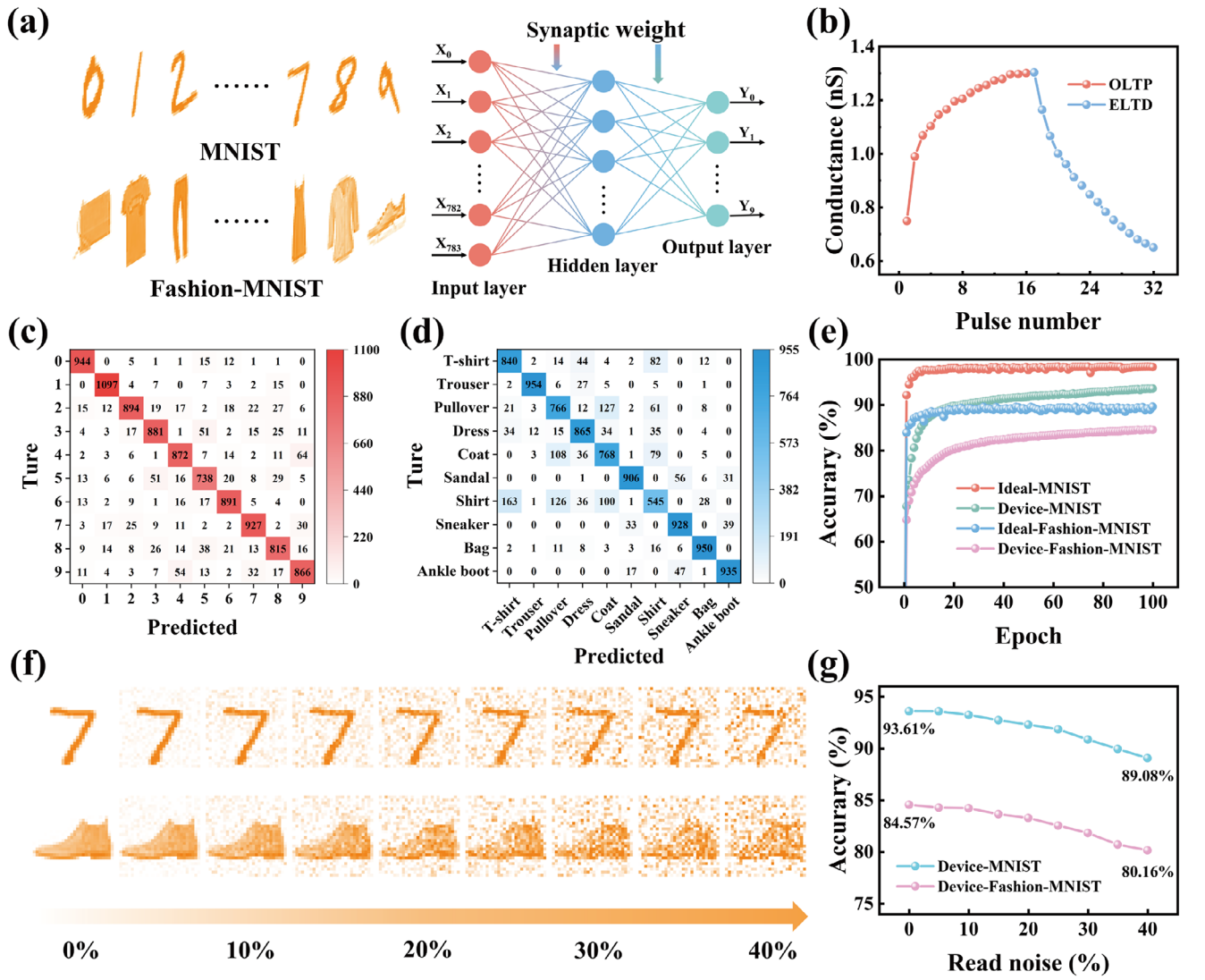

FIGURE 4 | Image recognition performance based on ANN. (a) Schematic diagram of the ANN architecture, consisting of 784 input neurons, 512 hidden neurons, and 10 output neurons, used for classification tasks on the MNIST and Fashion-MNIST datasets. (b) Photo-electrical dual-mode synaptic plasticity with LTP induced by 16 optical pulses (λ = 405 nm, optical power density = 6.5 mW cm^{-2}, pulse width = 0.3 s, pulse interval = 0.3 s) and LTD induced by 16 electrical pulses (pulse amplitude = 8 V, pulse width = 0.5 s, pulse interval = 0.5 s). (c) Confusion matrix of the MNIST dataset after 100 training cycles with weight updates extracted from device characteristics. (d) Confusion matrix of the Fashion-MNIST dataset after 100 training cycles with device-specific weight updates. (e) Comparison of recognition accuracy between the $NbOI_2$-based three-terminal optoelectronic synapse devices and idealized devices over 100 training cycles. (f) Representative image samples at different noise levels. (g) Recognition accuracy after 100 training cycles under different noise levels for MNIST and Fashion-MNIST datasets.

of 4.53%, while the accuracy decreased from 84.57% to 80.16% with a drop of 4.41% for the Fashion-MNIST dataset (Figure 4g). The evolution of classification accuracy as a function of training epoch with noise intensities at 0%, 20%, and 40% is further illustrated in Figure S15a,b for MNIST and Fashion-MNIST, respectively. These results demonstrate that the ANN exhibits robust recognition performance even under substantial noise perturbations, highlighting the reliability of the $NbOI_2$-based opto-electronic synapses for practical neuromorphic computing applications.

The results demonstrate that ANN constructed based on the $NbOI_2$-based three-terminal photonic synapse devices not only achieves efficient classification on standard benchmark datasets but also maintains stable performance under noisy environments. These findings fully validate the practical potential of such devices as vital building blocks for next-generation neuromorphic computing systems.

2.5 | Closed-Loop Vision-Motor Control and Multi-Degree-of-Freedom Human-Computer Interaction Based on the $NbOI_2$ Optoelectronic Synapses

To further validate the application of the $NbOI_2$ devices in real-world scenarios for its synaptic memory and temporal integration, a closed-loop human-computer interaction system inspired by the biological "vision-neural-motor" pathway was designed and implemented [59–63]. In this system, a front-end binocular

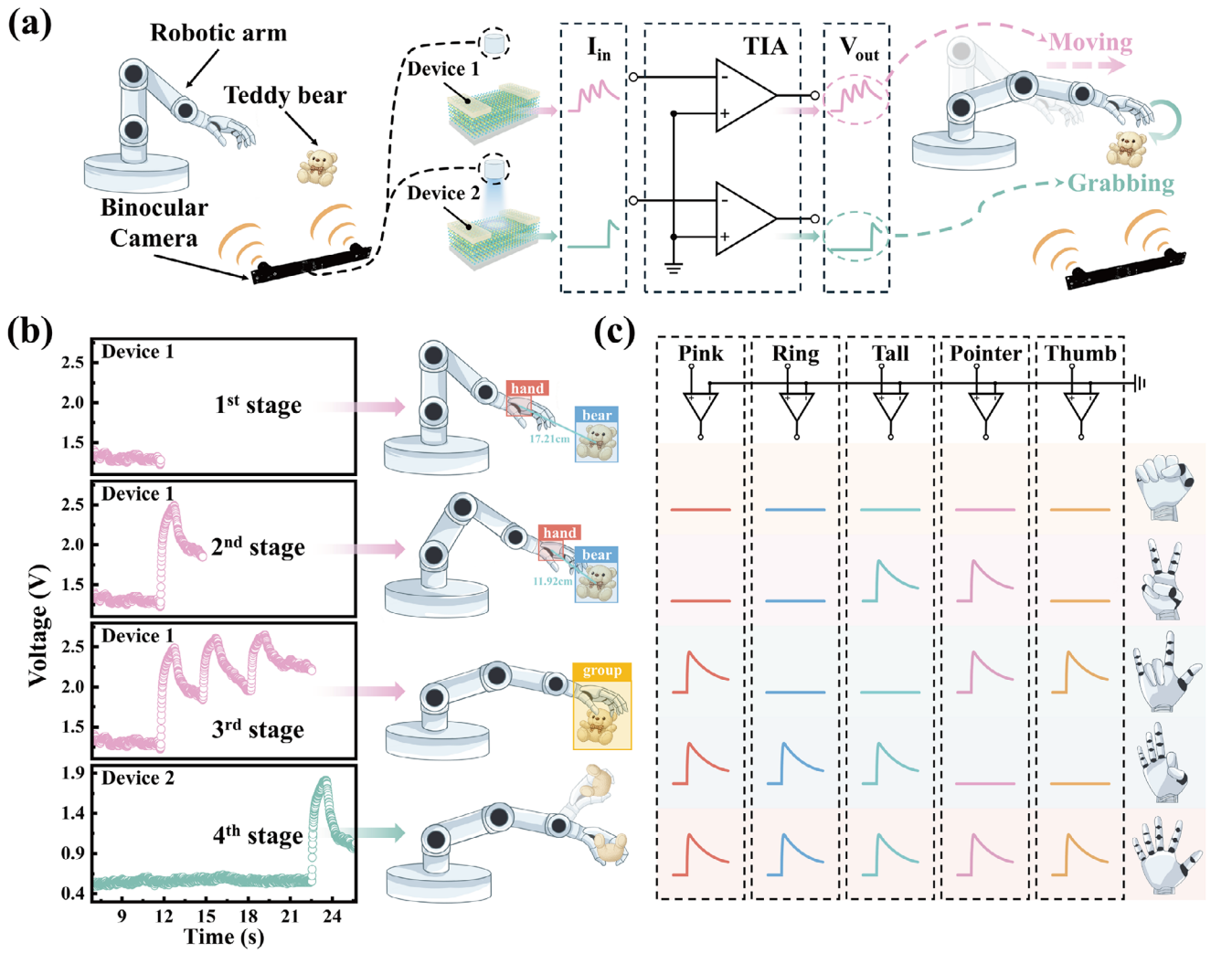

FIGURE 5 | Closed-loop vision-motor control and multi-degree-of-freedom human-computer interaction based on the $NbOI_2$ optoelectronic synapses. (a) Schematic illustration of the closed-loop interactive system architecture inspired by biological vision-neural-motor pathways. (b) Dynamic demonstration of the grasping process. The left panel shows the voltage signal converted by TIA as a function of time, while the right panel depicts real-time target identification using a stereo camera combined with the YOLO-v8 neural network on the computer. (c) Demonstration of multi-channel scalability that five independent "device-TIA" channels drive the five fingers of the robotic hand, enabling transformations from a fist posture to multiple predefined gestures.

camera paired with the YOLO-v8 neural network functioned as the "eye-brain," enabling real-time detection and localization of both target objects and the robotic hand's palm. Two $NbOI_2$ optoelectronic synaptic devices served as the "neural synapses," responsible for converting and transmitting sensory signals. A transimpedance amplifier (TIA) (gain = 10^{10} V/A, bandwidth = 10 kHz) and a stepper motor-driven robotic arm acted as the "motor effectors." The system employed an STM32 microcontroller as the central control unit, which was used to acquire and process current signals amplified by the TIA along with positional data transmitted from the front end, and subsequently to generate control commands to drive robotic arm movements. Through this integrated process, the system established a closed-loop perception-decision-execution-reperception control chain, effectively emulating biological sensorimotor pathways.

Real-time recognition and estimated distances were conducted by binocular camera and the YOLO-v8 neural network. As illustrated in Figure 5a, the binocular camera captured scene images and the YOLO-v8 neural network performed real-time recognition and bounding-box detection of the "robotic hand" and the "target object (doll)" on a computer, which output their relative positions and estimated distances on the image plane. When the system judged that the target object was within the reachable range of the robotic hand, the microcontroller triggered light pulses from the illumination source to stimulate $NbOI_2$ synapse 1 and $NbOI_2$ synapse 2, respectively. The photocurrent generated by synapse 1 was converted into a voltage signal through the TIA. Once this voltage exceeded a predefined threshold, A forward step distance of the robotic arm was calculated according to a pre-calibrated transfer function to adjust the extension distance of the arm. Similarly, the photocurrent generated in synapse 2 was converted into a voltage signal through the TIA. When this signal surpassed the threshold, it triggered the grasping action. These two synapses signals acted in sequence to enable sequential execution of "approaching the target" and "grasping the target."

Dynamic details of the grasping process were illustrated in Figure 5b. The left panel shows the voltage signals amplified by TIA, while the right panel presents the computer-calibrated real-time image generated by the binocular camera system combined with the YOLO-v8 network. When the target was absent, the outputs of the $NbOI_2$ synapse 1 and the $NbOI_2$ synapse 2 exhibited only minor fluctuations, and only "palm" and "doll" objects were calibrated in the image recognition module dependently. When a target object (doll) entered, the system applied optical pulses to $NbOI_2$ synapse 1. The EPSC from $NbOI_2$ synapse 1 was converted into a voltage signal by TIA, whose peak magnitude was mapped to the rotation angle of the stepper motor and drove the robotic arm closer to the target. If grasping conditions remained unreached, the system continued to apply light pulses to synapse 1. Benefiting from the synaptic memory effect, accumulated current was employed to accelerate, amplify progressively the voltage peak and enable the robotic arm to approach the target. Once the "palm-doll" unit was identified to an appropriate distance satisfying grasping conditions, the system stimulated $NbOI_2$ synapse 2 immediately by a light pulse. The voltage output from synapse 2 triggered the robotic hand to close and complete the grasp. Then, the system commanded the robotic hand to lift the target (Video S1). This closed-loop iteration that "visual feedback → synaptic accumulation → step control → re-recognition" enables the system to autonomously execute approach and grasping operations.

To evaluate the scalability of the $NbOI_2$ synapses in multi-channel motion control, a five-channel device-TIA configuration was established, corresponding to the five fingers of the robotic hand [64–66]. In the absence of stimulation, the robotic hand maintained a fist posture. When an optical pulse stimulated a given synapses, EPSC was generated and transferred to voltage output by TIA, corresponding to extended fingers. By selectively stimulating different combinations of synapses channels, the robotic hand was able to execute predefined gesture transition sequences, such as changing from a fist to an "OK" hand (Figure 5c; Video S2). The experimental evidence highlights the programmability and scalability of $NbOI_2$-based synaptic devices for multi-degree-of-freedom parallel motion control, thereby confirming their potential in complex human-computer interaction scenarios.

This section demonstrates the application of the $NbOI_2$-based optoelectronic synaptic in a "see-move-grasp" closed-loop architecture at the system level. Environmental perception and state judgement were realized by binocular vision and target detection. And synapse outputs were converted into effective control signals by the TIA, where the intrinsic memory characteristics of synapse enabled adaptive acceleration during the approach process to achieve arrival determination and perform grasp execution. By constructing a five-channel "synapse-TIA" pathway, both independent and coordinated finger actuation were realized without reliance on a visual recognition module. These results demonstrate that the proposed $NbOI_2$ synapse and system architecture not only support pattern recognition tasks at the algorithmic level (Figure 4) but also deliver stable and reusable perception-control integration in practical human-computer interaction scenarios. This result provides a viable pathway for hardware platforms targeting neuromorphic vision and intelligent human-machine collaboration.

3 | Conclusion

We have systematically demonstrated the unique features and application of the 2D ferroelectric semiconductor $NbOI_2$ from materials, synapse to systems. By rational structural design and interface engineering, a three-terminal $NbOI_2$ synapse was achieved with gate-tunable inhibitory synaptic currents for the first time, where PPD was emulated successfully. An ultra-low energy consumption of 6.65 fJ was realized, which is comparable to biological synaptic energy. Concurrently, EPSC, PPF, and LTP/LTD were demonstrated with optical and electrical pulses. The efficient classification of the MNIST and Fashion-MNIST datasets with accuracies of 93.61% and 84.57% was obtained based on an ANN with the extracted weight update parameters from $NbOI_2$ synapse, validating the feasibility of $NbOI_2$ synapses for low-power neural network computing. Notably, a closed-loop human-computer interaction system was constructed inspired by the biological "vision-neural-motor" pathway, where visual perception was realized through binocular cameras and the YOLO-v8 neural network, $NbOI_2$ synapses that provided signal regulation and memory storage, and a robotic arm that executed approach and grasping actions. The outcomes of a continuous mapping from environmental perception and signal processing to motor execution confirmed the practical feasibility of $NbOI_2$ synapses in intelligent human-computer collaboration. Moreover, finger actuation was realized with establishing a five-channel "synapse-TIA" system, verifying the programmability of $NbOI_2$ synapses for multi-degree-of-freedom parallel motion control and gesture generation. Our work indicates that the $NbOI_2$-based optoelectronic synapses hold promising prospects for broad applications in edge computing, intelligent robotics, and brain-computer interfaces, underscoring their significance as a material and device platform for neuromorphic electronics.

4 | Experimental Section

4.1 | Device Fabrication

The heterostructures were fabricated using an all-dry transfer method. Bulk $NbOI_2$ crystals were mechanically exfoliated using blue adhesive tape, and the as-exfoliated $NbOI_2$ thin flakes were first transferred onto a transparent polydimethylsiloxane (PDMS) film. A relatively large $NbOI_2$ flake with a thickness of approximately 35 nm was then selected and transferred onto a flexible polyethylene terephthalate (PET) substrate with the assistance of a precision transfer stage and optical microscopy. Subsequently, graphene and hexagonal boron nitride (*h*-BN) flakes were transferred onto the $NbOI_2$ flake using the same dry-transfer technique, forming a vertically stacked $NbOI_2$/graphene/*h*-BN/graphene heterostructure. During each transfer step, the PET substrate was heated to 100°C for approximately 8 min to improve interfacial adhesion. Finally, silver paste was applied to one side of the graphene layer to form a metal electrode, followed by annealing on a hot plate at 115°C for 15 min to ensure a stable electrical contact. The resulting $NbOI_2$ channel had a channel length of approximately 29.4 μm and a channel width of approximately 8.8 μm. The graphene and hexagonal boron nitride flakes were purchased from Shanghai OnWay Technology Co.,

Ltd., bulk $NbOI_2$ crystals were obtained from Nanjing Mokena Nanotechnology Co., Ltd., and the silver paste (01H-1803) was purchased from Shenzhen SAIYA Electronic Paste Co., Ltd.

4.2 | Characterizations

The structural and morphological characterizations of the devices and $NbOI_2$ flakes were carried out using a field-emission scanning electron microscope (FE-SEM, Zeiss Sigma 500, Germany), an energy-dispersive X-ray spectrometer (EDS, X-Max N20, UK), an optical microscope (OM, Olympus BX43F, Japan), and an atomic force microscope (AFM, Bruker Dimension Icon, USA). Raman spectra were obtained with a confocal Raman spectrometer (Horiba iHR550, France) equipped with a 532 nm laser excitation source. X-ray diffraction (XRD) measurements were performed on a Bruker D8 Advance diffractometer (Germany) using Cu Kα radiation (λ = 1.5406 Å). The crystal structure and interfacial characteristics were further examined by scanning transmission electron microscopy (STEM) operated at an accelerating voltage of 300 kV (FEI Tecnai G2 F30, USA). Electrical performance measurements of the devices were conducted on a semiconductor parameter analyzer (Keithley 4200A-SCS, USA) with an integrated probe station (Lake Shore TTPX, USA). All characterization and measurements were performed under ambient conditions.

Acknowledgements

This study was financially supported by the National Natural Science Foundation of China (Nos. 52472153, 52572288, 52125205, 52532005, 5225039, 52192614), Guangxi Natural Science Foundation (Nos. 2025GXNSFAA069357), the special funding for Guangxi Bagui Youth Scholars (Ping Chen), National Key Research and Development (R&D) Program from Ministry of Science and Technology of China (No. 2024YFB3814100), Natural Science Foundation of Beijing Municipality (Nos. 2222088 and L223006), and Fundamental Research Funds for the Central Universities.

Conflicts of Interest

The authors declare no conflicts of interest.

Data Availability Statement

The data that support the findings of this study are available from the corresponding author upon reasonable request.

References

1. S. R. Ahmed, R. Baghdadi, M. Bernadskiy, et al., "Universal Photonic Artificial Intelligence Acceleration," *Nature* 640, no. 8058 (2025): 368–374, https://doi.org/10.1038/s41586-025-08854-x.

2. Y. Liu, J. Tao, Y. Mo, R. Bao, and C. Pan, "Ultrasensitive Touch Sensor for Simultaneous Tactile and Slip Sensing," *Advanced Materials* 36, no. 21 (2024): 2313857, https://doi.org/10.1002/adma.202313857.

3. P. Slade, C. Atkeson, J. M. Donelan, et al., "On human-in-the-Loop Optimization of Human–Robot Interaction," *Nature* 633, no. 8031 (2024): 779–788, https://doi.org/10.1038/s41586-024-07697-2.

4. Z. Wang, T. Wan, S. Ma, and Y. Chai, "Multidimensional Vision Sensors for Information Processing," *Nature Nanotechnology* 19, no. 7 (2024): 919–930, https://doi.org/10.1038/s41565-024-01665-7.

5. Z. Sun, S. Kvatinsky, X. Si, A. Mehonic, Y. Cai, and R. Huang, "A Full Spectrum of Computing-in-Memory Technologies," *Nature Electronics* 6, no. 11 (2023): 823–835, https://doi.org/10.1038/s41928-023-01053-4.

6. S. Dai, X. Liu, Y. Liu, et al., "Emerging Iontronic Neural Devices for Neuromorphic Sensory Computing," *Advanced Materials* 35, no. 39 (2023): 2300329, https://doi.org/10.1002/adma.202300329.

7. A. C. Murphy, M. A. Bertolero, L. Papadopoulos, D. M. Lydon-Staley, and D. S. Bassett, "Multimodal Network Dynamics Underpinning Working Memory," *Nature Communications* 11, no. 1 (2020): 3035, https://doi.org/10.1038/s41467-020-15541-0.

8. D. G. Roe, S. Kim, Y. Y. Choi, et al., "Biologically Plausible Artificial Synaptic Array: Replicating Ebbinghaus' Memory Curve With Selective Attention," *Advanced Materials* 33, no. 14 (2021): 2007782, https://doi.org/10.1002/adma.202007782.

9. Y. Chen, J. Xia, Y. Qu, et al., "Ephaptic Coupling in Ultralow-Power Ion-Gel Nanofiber Artificial Synapses for Enhanced Working Memory," *Advanced Materials* 37, no. 16 (2025): 2419013, https://doi.org/10.1002/adma.202419013.

10. J. H. Yoon, M.-K. Song, W. Ham, et al., "Proton-Modulated Resistive Switching in a Synapse-Like Tyrosine-Rich Peptide-Based Memristor," *Advanced Functional Materials* 35, no. 7 (2024): 2415222, https://doi.org/10.1002/adfm.202415222.

11. D. S. Assi, H. Huang, V. Karthikeyan, V. C. S. Theja, M. M. de Souza, and V. A. L. Roy, "Topological Quantum Switching Enabled Neuroelectronic Synaptic Modulators for Brain Computer Interface," *Advanced Materials* 36, no. 27 (2024): 2306254, https://doi.org/10.1002/adma.202306254.

12. P. Chen, J. Pan, W. Gao, et al., "Anisotropic Carrier Mobility from 2H WSe_2," *Advanced Materials* 34, no. 7 (2022): 2108615, https://doi.org/10.1002/adma.202108615.

13. X. Liu, W. Zhang, X. Zhang, et al., "Transparent Ultrahigh-molecular-weight Polyethylene/MXene Films with Efficient UV-absorption for Thermal Management," *Nature Communications* 15, no. 1 (2024): 3076, https://doi.org/10.1038/s41467-024-47432-z.

14. Z. Zhang, S. Huo, Q. Tian, et al., "Near-Perfect Standard Ternary Inverter Based on $MoTe_2$ Homojunction Anti-Ambipolar Transistor," *Advanced Functional Materials* 35, no. 29 (2025): 2424728, https://doi.org/10.1002/adfm.202424728.

15. M. Dong, Y. Zhang, J. Zhu, et al., "All-in-One 2D Molecular Crystal Optoelectronic Synapse for Polarization-Sensitive Neuromorphic Visual System," *Advanced Materials* 36, no. 40 (2024): 2409550, https://doi.org/10.1002/adma.202409550.

16. D. Wen, S. Zuo, C. Huang, et al., "Tunable Excitation Polarized Upconversion Luminescence and Reconfigurable Double Anti-Counterfeiting from Er 3+ Doped Single Nanorods," *Advanced Optical Materials* 11, no. 24 (2023): 2301126, https://doi.org/10.1002/adom.202301126.

17. Y.-L. He, J.-H. Yan, Y.-T. Yang, et al., "Achieving Enhanced Linear and Nonlinear Optical Absorption in a $(PEA)_2PbI_4/WS_2$ Heterojunction by Efficient Energy Transfer," *Rare Metals* 44, no. 8 (2025): 5877–5885, https://doi.org/10.1007/s12598-025-03299-7.

18. B. Pan, L. Zhang, S. Lan, et al., "General Synthesis Strategy of 2D Transition Metal Dichalcogenide Gradient Alloys for High-Performance Optoelectronic Synapses," *Advanced Functional Materials* 35, no. 23 (2025): 2421137, https://doi.org/10.1002/adfm.202421337.

19. Q. Chen, Y. Wei, P.-B. Zhai, and Y.-J. Gong, "Van der Waals Gap Engineering in 2D Materials for Energy Storage and Conversion," *Rare Metals* 43, no. 12 (2024): 6125–6143, https://doi.org/10.1007/s12598-024-02817-3.

20. W. Fan, H. Yan, X. Wang, et al., "Polarization-Sensitive Photosynapse Based on $PdSe_2/WS_2$ Heterostructure for Visible-Infrared Broadband Artificial Vision System," *Advanced Functional Materials* 35, no. 43 (2025): 2416703, https://doi.org/10.1002/adfm.202416703.

21. H. Liu, X. Chen, Y. Zheng, et al., "Lightweight, Superelastic, and Hydrophobic Polyimide Nanofiber/MXene Composite Aerogel for Wearable Piezoresistive Sensor and Oil/Water Separation Applications," *Advanced Functional Materials* 31, no. 13 (2021): 2008006, https://doi.org/10.1002/adfm.202008006.

22. Y. Fang, F. Wang, R. Wang, T. Zhai, and F. Huang, "2D $NbOI_2$: A Chiral Semiconductor with Highly In-Plane Anisotropic Electrical and Optical Properties," *Advanced Materials* 33, no. 29 (2021): 2101505, https://doi.org/10.1002/adma.202101505.

23. I. Abdelwahab, B. Tilmann, Y. Wu, et al., "Giant Second-harmonic Generation in Ferroelectric $NbOI_2$," *Nature Photonics* 16, no. 9 (2022): 644–650, https://doi.org/10.1038/s41566-022-01021-y.

24. C. Liu, X. Zhang, X. Wang, et al., "Ferroelectricity in Niobium Oxide Dihalides $NbOX_2$ (X = Cl, I): A Macroscopic- to Microscopic-scale Study," *ACS Nano* 17, no. 8 (2023): 7170–7179, https://doi.org/10.1021/acsnano.2c09267.

25. D.-P. Wen, P. Chen, Y. Liang, X.-M. Mo, and C.-F. Pan, "Regulated Polarization Degree of Upconversion Luminescence and Multiple Anti-Counterfeit Applications," *Rare Metals* 43, no. 5 (2024): 2172–2183, https://doi.org/10.1007/s12598-024-02675-z.

26. X. Sun, Y. Wan, Y. Fang, and F. Huang, "Layered Ferroelectric NbOI 2 Flakes Toward In-Plane Anisotropic Self-Powered Sensing," *Small Science* 4, no. 2 (2023): 2300125, https://doi.org/10.1002/smsc.202300125.

27. Y. Cui, T. Wang, D. Hu, Z. Wang, J. Hong, and X. Wang, "Piezoelectricity in $NbOI_2$ for Piezotronics and Nanogenerators," *npj 2D Materials and Applications* 8, no. 1 (2024): 62, https://doi.org/10.1038/s41699-024-00498-1.

28. T. Handa, C.-Y. Huang, Y. Li, et al., "Terahertz Emission from Giant Optical Rectification in a Van Der Waals Material," *Nature Materials* 24, no. 8 (2025): 1203–1208, https://doi.org/10.1038/s41563-025-02201-1.

29. X. Huang, Q. Wang, K. Song, et al., "In-Plane Bulk Photovoltaic Effect in a $MoSe_2/NbOI_2$ Heterojunction for Efficient Polarization-Sensitive Self-Powered Photodetection," *Nano Letters* 25, no. 4 (2025): 1495–1503, https://doi.org/10.1021/acs.nanolett.4c05418.

30. M. Wang, D. Ouyang, Y. Dai, et al., "2D Piezo-Ferro-Opto-Electronic Artificial Synapse for Bio-Inspired Multimodal Sensory Integration," *Advanced Materials* 37, no. 24 (2025): 2500049, https://doi.org/10.1002/adma.202500049.

31. D. Ouyang, M. Wang, N. Zhang, et al., "2D Time-Stretching Anisotropic Synapse Realizing In-Sensor Intensity-Spanning Visual Feature Fusion," *Advanced Materials* 37, no. 33 (2025): 2507168, https://doi.org/10.1002/adma.202507168.

32. K. He, Y. Liu, J. Yu, et al., "Artificial Neural Pathway Based on a Memristor Synapse for Optically Mediated Motion Learning," *ACS Nano* 16, no. 6 (2022):9691–9700, https://doi.org/10.1021/acsnano.2c03100.

33. H. Wang, Q. Chen, Y. Cao, et al., "Anisotropic Strain-Tailoring Nonlinear Optical Response in Van Der Waals $NbOI_2$," *Nano Letters* 24, no. 11 (2024): 3413–3420, https://doi.org/10.1021/acs.nanolett.4c00039.

34. Q. Yan, Y. Weng, S. Wang, et al., "Ambient Degradation Anisotropy and Mechanism of van der Waals Ferroelectric $NbOI_2$," *ACS Applied Materials & Interfaces* 16, no. 7 (2024): 9051–9059, https://doi.org/10.1021/acsami.3c18018.

35. R. Wang, X. Yuan, S. Lin, et al., "Tailoring the Charge Transfer-Driven Oxidation in Van Der Waals Ferroelectric $NbOI_2$ Through Hetero-Interface Engineering," *Advanced Functional Materials* 35, no. 6 (2024): 2414753, https://doi.org/10.1002/adfm.202414753.

36. H. Ahn, Y. Kim, S. Seo, et al., "Artificial Optoelectronic Synapse Featuring Bidirectional Post-Synaptic Current for Compact and Energy-Efficient Neural Hardware," *Advanced Materials* 37, no. 34 (2025): 2418582, https://doi.org/10.1002/adma.202418582.

37. J. Wang, N. Ilyas, Y. Ren, et al., "Technology and Integration Roadmap for Optoelectronic Memristor," *Advanced Materials* 36, no. 9 (2023): 2307393, https://doi.org/10.1002/adma.202307393.

38. A. Goto, A. Bota, K. Miya, et al., "Stepwise Synaptic Plasticity Events Drive the Early Phase of Memory Consolidation," *Science* 374, no. 6569 (2021): 857–863, https://doi.org/10.1126/science.abj9195.

39. A. J. Arnold, A. Razavieh, J. R. Nasr, D. S. Schulman, C. M. Eichfeld, and S. Das, "Mimicking Neurotransmitter Release in Chemical Synapses via Hysteresis Engineering in MoS_2 Transistors," *ACS Nano* 11, no. 3 (2017): 3110–3118, https://doi.org/10.1021/acsnano.7b00113.

40. J. Shu, G. Wu, Y. Guo, B. Liu, X. Wei, and Q. Chen, "The Intrinsic Origin of Hysteresis in MoS_2 Field Effect Transistors," *Nanoscale* 8, no. 5 (2016): 3049–3056, https://doi.org/10.1039/c5nr07336g.

41. D. Tan, Z. Zhang, H. Shi, et al., "Bioinspired Artificial Visual-Respiratory Synapse as Multimodal Scene Recognition System with Oxidized-Vacancies MXene," *Advanced Materials* 36, no. 36 (2024): 2407751, https://doi.org/10.1002/adma.202407751.

42. Y. Wang, W. Shan, H. Li, et al., "An Optoelectrochemical Synapse Based on a Single-Component n-type Mixed Conductor," *Nature Communications* 16, no. 1 (2025): 1615, https://doi.org/10.1038/s41467-025-56814-w.

43. Z. Liu, Y. Wang, Y. Zhang, et al., "Harnessing Defects in SnSe Film via Photo-Induced Doping for Fully Light-Controlled Artificial Synapse," *Advanced Materials* 37, no. 4 (2024): 2410783, https://doi.org/10.1002/adma.202410783.

44. Z. Lian, J. Wei, Y. Liu, et al., "Highly Responsive Dual-function Deep-ultraviolet Neuromorphic Phototransistors Based on Silicon Carbide Nanoparticle/2D MoS_2 Heterostructures," *ACS Nano* 19, no. 28 (2025): 26041–26054, https://doi.org/10.1021/acsnano.5c06692.

45. Y. Yu, L. Zhang, Y. Zheng, et al., "Artificial Optoelectronic Synapse Based on 18R-Phase $SnSe_2$ for Neuromorphic Computing," *Laser & Photonics Reviews* 19, no. 14 (2025): 2500214, https://doi.org/10.1002/lpor.202500214.

46. J. Sung, S. W. Kim, D. Lee, S. Moon, E. Lee, and H. H. Kim, "Co-Stimuli-Driven 2D WSe_2 Optoelectronic Synapses for Neuromorphic Computing," *Small* 21, no. 31 (2025): 2504024, https://doi.org/10.1002/smll.202504024.

47. S. S. Han, C. W. Lee, C. Yoo, et al., "Wafer-scale Flexible 2D $PtSe_2$ Layers with bi-directional Wavelength Tunability for Fully Optical Synaptic Operations," *Nano Energy* 139, no. 15 (2025): 110943, https://doi.org/10.1016/j.nanoen.2025.110943.

48. Z. Shang, L. Liu, G. Wang, et al., "Ferroelectric Polarization Enhanced Optoelectronic Synaptic Response of a $CuInP_2S_6$ Transistor Structure," *ACS Nano* 18, no. 44 (2024): 30530–30539, https://doi.org/10.1021/acsnano.4c08810.

49. Y. Zhao, W. Gao, K. Dai, et al., "Bioinspired Multifunctional Photonic-Electronic Smart Skin for Ultrasensitive Health Monitoring, for Visual and Self-Powered Sensing," *Advanced Materials* 33, no. 45 (2021): 2102332, https://doi.org/10.1002/adma.202102332.

50. Q. Li, T. Wang, Y. Fang, et al., "Ultralow Power Wearable Organic Ferroelectric Device for Optoelectronic Neuromorphic Computing," *Nano Letters* 22, no. 15 (2022): 6435–6443, https://doi.org/10.1021/acs.nanolett.2c01768.

51. H. Xiong, L. Xu, C. Gao, et al., "Optically Modulated HfS_2-based Synapses for Artificial Vision Systems," *ACS Applied Materials & Interfaces* 13, no. 42 (2021): 50132–50140, https://doi.org/10.1021/acsami.1c14332.

52. Y. Wang, B. Han, M. Mayor, and P. Samorì, "Opto-Electrochemical Synaptic Memory in Supramolecularly Engineered Janus 2D MoS_2," *Advanced Materials* 36, no. 8 (2023): 2307359, https://doi.org/10.1002/adma.202307359.

53. D. Kumar, H. Li, U. K. Das, A. M. Syed, and N. El-Atab, "Flexible Solution-Processable Black-Phosphorus-Based Optoelectronic Memristive Synapses for Neuromorphic Computing and Artificial Visual Perception Applications," *Advanced Materials* 35, no. 28 (2023): 2300446, https://doi.org/10.1002/adma.202300446.

54. W. Yang, S. Liu, Z. Wang, et al., "Bioinspired Composite fiber Aerogel Pressure Sensor for Machine-Learning-Assisted Human Activity and Gesture Recognition," *Nano Energy* 127, (2024): 109799, https://doi.org/10.1016/j.nanoen.2024.109799.

55. Y. Zheng, T. Liu, J. Wu, et al., "Energy Conversion Analysis of Multilayered Triboelectric Nanogenerators for Synergistic Rain and Solar Energy Harvesting," *Advanced Materials* 34, no. 28 (2022): 2202238, https://doi.org/10.1002/adma.202202238.

56. X. Han, J. Tao, Y. Liang, et al., "Ultraweak Light-modulated Heterostructure with Bidirectional Photoresponse for Static and Dynamic Image Perception," *Nature Communications* 15, no. 1 (2024): 10430, https://doi.org/10.1038/s41467-024-54845-3.

57. J. Sun, S. Oh, Y. Choi, et al., "Optoelectronic Synapse Based on IGZO-Alkylated Graphene Oxide Hybrid Structure," *Advanced Functional Materials* 28, no. 47 (2018): 1804397, https://doi.org/10.1002/adfm.201804397.

58. T. Zhao, C. Zhao, W. Xu, et al., "Bio-Inspired Photoelectric Artificial Synapse based on Two-Dimensional Ti_3 C_2 T x MXenes Floating Gate," *Advanced Functional Materials* 31, no. 45 (2021): 2106000, https://doi.org/10.1002/adfm.202106000.

59. J. He, R. Wei, X. Ma, et al., "Contactless User-Interactive Sensing Display for Human–Human and Human–Machine Interactions," *Advanced Materials* 36, no. 25 (2024): 2401931, https://doi.org/10.1002/adma.202401931.

60. C. Pan, J. Zhai, and Z. Wang, "Piezotronics and Piezo-phototronics of Third Generation Semiconductor Nanowires," *Chemical Reviews* 119, no. 15 (2019): 9303–9359, https://doi.org/10.1021/acs.chemrev.8b00599.

61. M. Qi, R. Yang, Z. Wang, et al., "Bioinspired Self-healing Soft Electronics," *Advanced Functional Materials* 33, no. 17 (2021): 2214479, https://doi.org/10.1002/adfm.202214479.

62. Y. Zhao, R. Wu, Y. Hao, et al., "Eco-Friendly Multifunctional Hydrogel Sensors Enabled Sustainable and Accurate Human-Machine Interaction System," *Advanced Materials* 37, no. 32 (2025): 2507127, https://doi.org/10.1002/adma.202507127.

63. G. Gao, F. Yang, F. Zhou, et al., "Bioinspired Self-Healing Human–Machine Interactive Touch Pad with Pressure-Sensitive Adhesiveness on Targeted Substrates," *Advanced Materials* 32, no. 50 (2020): 2004290, https://doi.org/10.1002/adma.202004290.

64. S. Yang, W. Yang, R. Yin, et al., "Waterproof Conductive Fiber with Microcracked Synergistic Conductive Layer for High-Performance Tunable Wearable Strain Sensor," *Chemical Engineering Journal* 453, no. 1 (2023): 139716, https://doi.org/10.1016/j.cej.2022.139716.

65. Y. Zhang, Q. Lu, J. He, et al., "Localizing Strain via Micro-cage Structure for Stretchable Pressure Sensor Arrays with Ultralow Spatial Crosstalk," *Nature Communications* 14, no. 1 (2023): 1252, https://doi.org/10.1038/s41467-023-36885-3.

66. X. Wang, Y. Zhang, X. Zhang, et al., "A Highly Stretchable Transparent Self-Powered Triboelectric Tactile Sensor with Metallized Nanofibers for Wearable Electronics," *Advanced Materials* 30, no. 12 (2018): 1706738, https://doi.org/10.1002/adma.201706738.

Supporting Information

Additional supporting information can be found online in the Supporting Information section.

Supporting File 1: adfm74504-sup-0001-SuppMat.docx.

Supporting File 2: adfm74504-sup-0002-VideoS1.mp4.

Supporting File 3: adfm74504-sup-0003-VideoS2.mp4.